journal

J. Am. Ceram. Soc., **80** [6] 1341–52 (1997)

"Classical" Superplasticity of SiAlON Ceramics

Anatoly Rosenflanz* and I-Wei Chen*

Department of Materials Science and Engineering, University of Michigan, Ann Arbor, Michigan 48109

"Classical" superplasticity of SiAlON ceramics with the nominal composition $(Y_xLi_y)_{0.6/(3x+y)}Si_{8.9}Al_{3.1}O_{2.5}N_{13.5}$ is reported in this study. During deformation, these materials exhibit little microstructural evolution, with negligible growth of elongated β′-phase grains and minimal texture formation. Excellent formabilities are obtained in the temperature range of 1500°–1600°C in compression, where a strain rate of 10^{-2} s^{-1} has been achieved, and in punch stretching, where a strain rate of 1.2×10^{-3} s^{-1} has been used successfully. Flow stresses are found to be dramatically affected by the viscosity of the grain-boundary phase and decrease as the amount of lithium addition increases. Fracture stress also is compositionally dependent and decreases as the lithium content increases. As the overall formability is determined by the competition between fracture and deformation, maximum formability coincides with a maximum ratio of fracture stress to forming stress at an intermediate lithium composition. Finally, all materials exhibit higher room-temperature bend strength after postforming annealing. Thus, transient superplastic deformation does not impair the ultimate mechanical properties of the materials.

I. Introduction

In CERAMICS, superplastic forming has been a subject of considerable interest as a novel method of net-shape fabrication of parts. Promising results were first achieved for β-spodumene (β-$LiAlSi_2O_6$) glass ceramics[1] and later for Y_2O_3-stabilized tetragonal ZrO_2,[2] Al_2O_3,[3] and some other oxide composites.[4] Efforts also were made to establish superplasticity in Si_3N_4 and related SiAlON ceramics, which exhibit outstanding mechanical properties. Superplasticity in these ceramics was first found in Si_3N_4/SiC composites, for which uniform superplastic elongation (>150%) was achieved in tension.[5] Later, a wide range of SiAlON materials with compositions lying on the α′-plane (a plane in the "Janecke prism," where all compositions can be described by the general formula $Me_xSi_{12-(m+n)}Al_{m+n}O_nN_{16-n}$, with Me being a metal cation) were rendered superplastic in uniaxial[6] and biaxial[4,7] stretching experiments. In all the above-mentioned work, however, complex phase and microstructural evolutions of the Si_3N_4-based ceramics were evident. These typically involved α- → β-Si_3N_4 and α′ → β′-SiAlON phase transformation, compositional changes in the grain-boundary liquid phase, and grain growth of anisotropic β- or β′-phase grains. In some cases, pronounced strain hardening due to these evolutions has been observed.[6] Moreover, although the presence of fiberlike grains was generally detrimental for ceramic superplasticity,[8] in Si_3N_4 materials, their formation is largely *in situ* and they tend to align with the tensile stress field, producing a fiber-strengthening effect; this, in turn, seems to have significantly extended the ductility of such materials.[6,7] In this sense, the superplastic deformation of those Si_3N_4 ceramics which lack an equiaxed micrograin structure can be termed "nonclassical."

Polycrystalline β′-SiAlON normally forms from α-Si_3N_4 through a solution–reprecipitation process. The temperature dependence of such a transformation displays a sigmoidal curve, which is typical for these materials[9] (Fig. 1). During the initial stages of this transformation, a large driving force is probably present. In theory, this should favor isotropic growth by promoting rough interfaces, thereby avoiding the formation of elongated grains, which are commonly found in later stages of transformation when only a lower driving force remains.[10] Therefore, an important conclusion may be drawn, namely that β′-phase anisotropic grain growth can be prevented if densification and superplastic deformation proceed in either the initial or intermediate stages of the phase transformation process. That is, the left-hand side of the transformation curve in Fig. 1 provides a window of opportunity for "classical" superplasticity.

In this work, we have successfully exploited this processing window for classical superplasticity in Si_3N_4 materials. Full densification is achieved with only a small fraction of α-phase converted to β′-SiAlON phase, and the microstructure is characterized by fine, equiaxed grains during the entire history of superplastic forming. Moreover, we are able to maintain a comparable grain size and α-to-β′ conversion ratio in a series of Si_3N_4 materials while varying the viscosity of the grain-boundary phase by adjusting the proportion of two sintering additives—Li_2O and Y_2O_3. Without complications that result from different extents of α → β′-SiAlON phase transformation and the *in-situ* formation of a large number of elongated β′-SiAlON grains, diffusion-controlled solution–reprecipitation creep should operate in superplastic deformation, and it should be characterized by a strong dependence of the operating flow stress on the grain size and viscosity of the grain-boundary liquid phase.[1] Furthermore, ductility and formability should be controlled by

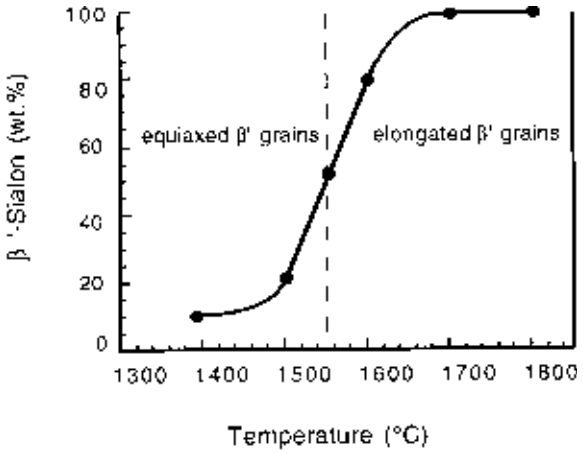

Fig. 1. Formation of β′-SiAlON phase versus hot-pressing temperature, showing the sigmoidal behavior usually observed for these materials. ($Y_{1.0}Li_0$ composition hot pressed under a pressure of 40 MPa.

R. Raj—contributing editor

Manuscript No. 191686. Received July 10, 1996; approved December 2, 1996.

Supported by the U.S. Air Force Office for Scientific Research under Grant Nos. AFOSR-F49620-95-1-0119 and F49620-95-1-0460.

Presented at the 97th Annual Meeting of the American Ceramic Society (May 1, 1995, Cincinnati, OH), Paper No. SXX-07.

*Member, American Ceramic Society.

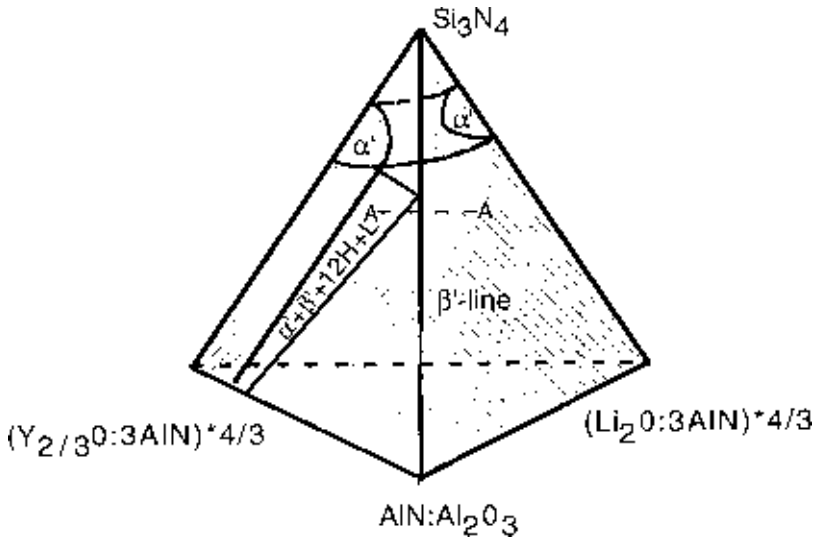

Fig. 2. Tetrahedron representing the α′-SiAlON phase field when two interstitial cations—lithium and yttrium—are used; the two front faces are the yttrium–α′-SiAlON plane and the lithium–α′-SiAlON plane. Studied compositions lie along the A–A line.

the ratio of flow stress to fracture stress, as suggested by Chen and Xue.[4]

II. Experimental Procedure

(1) Material

(A) Composition: SiAlON materials with two interstitial cations (yttrium and lithium) were chosen for investigation. With two interstitial cations, the composition of α′-SiAlON in the general formula $(Y_xLi_y)_{m/(y+3x)}Si_{12-(m+n)}Al_{m+n}O_nN_{16-n}$ may be represented by a tetrahedron (Fig. 2) in which the two front faces are the α′-phase planes for yttrium–SiAlON and lithium–SiAlON. The compositions that we studied in this work all lie along the A–A line (Fig. 2) and have the following values: $m = 0.6$, $n = 2.5$. These materials have been designated as Y_xLi_y in this study.

(B) Powder Processing: Initial powders (α-Si_3N_4 (UBE 10, UBE Industries, Yamaguchi, Japan), Al_2O_3 (AKP50, Sumitomo Chemical America), AlN (Type F, Tokuyama Soda Co., Tokyo, Japan), Y_2O_3 (Aldrich Chemical Co., Milwaukee, WI), and Li_2O (Aldrich Chemical Co.)) were mixed in appropriate proportions to achieve the desired composition, after considering the residual oxygen content of Si_3N_4 and AlN (Table I). The powder mixture, in batches of 40 g, was attrition milled in isopropyl alcohol for 2 h using high-purity Si_3N_4 milling media in a Teflon™-coated (E. I. DuPont de Nemours Co., Wilmington, DE) jar. The slurry was subsequently dried under a lamp while being stirred.

(C) Hot Pressing: Charges of 10 g each were initially cold pressed into green-body compacts before hot pressing. Hot pressing was performed in a nitrogen atmosphere in a graphite resistance furnace. The initial heating rate was 25°C/min up to 1000°C, followed by a slower rate of 15°C/min to the desired temperature. After the completion of densification, the furnace was shut down to allow rapid cooling at a typical cooling rate of 100°C/min to 1000°C. In the above-mentioned procedure, load was applied when the temperature first attained 1000°C and was maintained at a constant value of 40 MPa during the densification stage. During cooling, the load was released at 1000°C.

Temperatures and holding times were systematically varied to obtain materials with the lowest amount of α → β′ phase transformation. The parameters that were used to obtain the materials that are studied here are shown in Table II. These materials include a series of compositions in which the lithium content in Y_xLi_y varied in the range of 0–100 at.%, with essentially the same α-/β′-phase conversion ratio of ~25%. The parameters shown in Table II generally reflect a trend of easier densification and α → β′ phase transformation with increasing lithium content; that is, a lower temperature and a shorter holding time are needed to obtain the same final density and phase assemblage.

(2) Deformation

The superplastic formability of the investigated materials was assessed by uniaxial compression and biaxial punch-stretching tests. Specimens were machined from dense hot-pressed material. The final specimen dimensions were 3 mm × 3 mm × 6 mm for compression tests and 34 mm (diameter) × 1.2 mm (thickness) for punch-stretching tests. These experiments were performed under a nitrogen atmosphere in a resistance furnace with a tungsten heating element. Prior to testing, a heating rate of 30°C/min was used for heating to testing temperature.

Uniaxial compression tests were performed by pressing specimens between two SiC platens in a servohydraulic mechanical tester (MTS Systems Corp., Minneapolis, MN). Thin graphite foils were placed between the SiC platens and the specimens to reduce friction. A constant strain rate was maintained by advancing the crosshead at a decreasing speed to compensate

Table I. Compositions of Powder Mixtures

	Composition (wt%)				
Material	Si_3N_4	AlN	Y_2O_3	Li_2O	Al_2O_3
$Y_{1.0}Li_0$	72.12	13.86	3.89		10.13
$Y_{0.8}Li_{0.2}$	72.25	13.88	3.6	0.12	10.14
$Y_{0.75}Li_{0.25}$	72.29	13.89	3.5	0.16	10.15
$Y_{0.66}Li_{0.33}$	72.36	13.91	3.35	0.22	10.16
$Y_{0.5}Li_{0.5}$	72.55	13.94	2.93	0.39	10.19
$Y_{0.25}Li_{0.75}$	72.98	14.03	1.97	0.78	10.24
$Y_0Li_{1.0}$	73.85	14.2		1.58	10.37

Table II. Hot-Pressing Parameters and Amount of β′-SiAlON Formation

Material	Temperature (°C)	Holding time (min)	Applied pressure (MPa)	β′-SiAlON amount (wt%)
$Y_{1.0}Li_0$	1550	5	27	34
$Y_{1.0}Li_0$	1520	7	35	30
$Y_{1.0}Li_0$	1480	10	35	25
$Y_{1.0}Li_0$	1470	15	40	22
$Y_{1.0}Li_0$	1460	20	40	22
$Y_0Li_{1.0}$	1410	30	40	25
$Y_{0.8}Li_{0.2}$	1460	8	40	25
$Y_{0.75}Li_{0.25}$	1430	30	40	25
$Y_{0.66}Li_{0.33}$	1420	30	40	24
$Y_{0.25}Li_{0.75}$	1410	40	40	25

for the decrease in the gauge length of the specimen. For biaxial punch stretching, the test piece was clamped between two circular concentric graphite dies with an inner radius of 8 mm. The disk was stretched by advancing a hemispherical punch (radius of 6 mm) at a constant speed. A detailed description of the biaxial punch-stretching process can be found in Wu and Chen.[11]

(3) Phase, Microstructure, and Characterization

(A) Phases and Microstructure: As-hot-pressed and as-deformed materials were subjected to annealing to establish the equilibrium phase assemblage. This heat treatment was performed in a graphite resistance furnace under ~0.1 MPa (1 atm) of nitrogen at 1700°C for 3 h.

X-ray diffractometry (XRD) (using Cu*K*α radiation), scanning electron microscopy (SEM), and light microscopy were used for phase identification and microstructural characterization. To estimate the amounts of various phases, the procedure for quantitative XRD analysis, as described by Gazzara and Messier,[12] was followed. To avoid the effect of texture on XRD patterns, this analysis was conducted using pulverized powders. Specimens for SEM examination were broken at room temperature to reveal their microstructure.

(B) Microhardness and Bend Strength: The microhardness of various as-hot-pressed materials was measured with a Vickers diamond indenter under an applied load of 98 N. The strength was measured at room temperature in three-point bending using a SiC fixture. Before testing, the surface was polished using a diamond paste to remove residual stresses.

III. Results

(1) Phase and Microstructure Development

At thermodynamic equilibrium, materials with the investigated compositions contain mostly β′-SiAlON, in addition to some α′-SiAlON, 12H ($Al_6O_3N_4$), and liquid phase. In this work, however, we have found that such a phase assemblage is attained only after postforming annealing at 1700°C for 3 h. (Of course, the equilibrium phase assemblage at lower temperatures may be somewhat different; however, the difference is expected to be relatively small, except for liquid and oxide phases.) Thus, a nonequilibrium phase assemblage exists in as-hot-pressed and as-deformed materials; this is illustrated in Fig. 3, which plots the percentage of equilibrium phase assemblage at three stages: after hot pressing, after forming, and after annealing. The relatively small (~25 wt%) α-/β′-SiAlON phase conversion ratio in the dense, hot-pressed materials, compared to that in previous studies,[10,13] is attributed to the lower hot-pressing temperature that has been used here and the kinetic limitations of α → β′-SiAlON phase transformation, which requires the dissolution of α-phase into grain-boundary phase, diffusion through this phase, and ultimate precipitation as the β′-SiAlON phase.[14] Later, during formation, the further advance in phase development is limited to ~50%, and thermodynamic equilibrium is attained only after annealing. The phase development is significantly influenced by material composition. As the amount of lithium in the composition increases, the phase evolution process accelerates (Table II).

Observations of fracture surfaces revealed that all the materials that have been studied here have similar grain sizes and morphologies after hot pressing. The typical microstructure mostly consisted of equiaxed grains with an average size of 0.1–0.3 μm. Although some coarsening of the microstructure was evident after deformation, the general grain morphology did not change substantially, again mostly composed of equiaxed grains with a typical grain size of 0.2–0.5 μm. Annealed materials, on the other hand, contained mostly elongated β′-SiAlON grains with a larger grain size (1–2 μm). Typical micrographs are shown in Fig. 4.

In the absence of a large proportion of elongated β′-phase grains, texturing of the grains is not expected. A comparison of the XRD patterns of materials in as-deformed and pulverized forms taken from the pole section of the punch-stretched dome (at a punch speed of 0.8 mm/min at 1585°C to a height of 10 mm) confirmed this point. As shown in Fig. 5, no significant texturing is evident in these XRD patterns.

(2) Deformation

Compression tests were performed at temperatures in the range of 1400°–1625°C and at strain rates (ε) in the range of 10^{-4}–10^{-2} s^{-1}; a single specimen was used for each ε value. A typical set of true stress–true strain curves for the $Y_{0.75}Li_{0.25}$ material is shown in Fig. 6. Strain hardening was minimal at low and intermediate ε values, except in the initial transient after loading. Thus, a relatively flat stress–strain curve was obtained. At very high ε values (up to 10^{-2} s^{-1} for the $Y_{0.66}Li_{0.33}$ material at 1625°C), deformation exhibited a "semiductile" behavior with a stress maximum in the stress–strain curve.

To compare flow stresses, we took their values after 300 s of deformation, to avoid the initial strain-hardening regions. At high ε values, when a true strain of 0.5 was achieved in <300 s, the flow stress was taken at a true strain of 0.5. Figure 7 shows the effect of material composition on flow stress. Flow stress at first decreases as the amount of lithium increases; later, in the lithium-rich compositions, the flow stress increases again. This increase is probably an artifact, because extensive strain hardening has occurred in the lithium-rich compositions, causing the flow stresses to increase continuously. A high rate of lithium and liquid loss from the surface of the specimen, which increases the liquid viscosity of the surface region, is believed to cause the observed strain hardening. Visual observation of lithium-rich compression specimens revealed the presence of multiple surface cracks, indicating that the surface flow stress had increased above the fracture stress as a result of lithium and liquid loss.

As in our earlier work,[7,15] compressive deformation of SiAlONs exhibited a transitional behavior. In the regime of low ε values, Newtonian flow with a stress exponent n ($n = \partial(\ln \varepsilon)/\partial(\ln \sigma) = 1$) occurred, whereas at high ε values, shear-thickening flow,[15] with $n = 0.5$, was observed (Fig. 8); this gives a concave-upward curvature of the σ–ε data shown in Fig. 8. The transition stress is composition dependent and

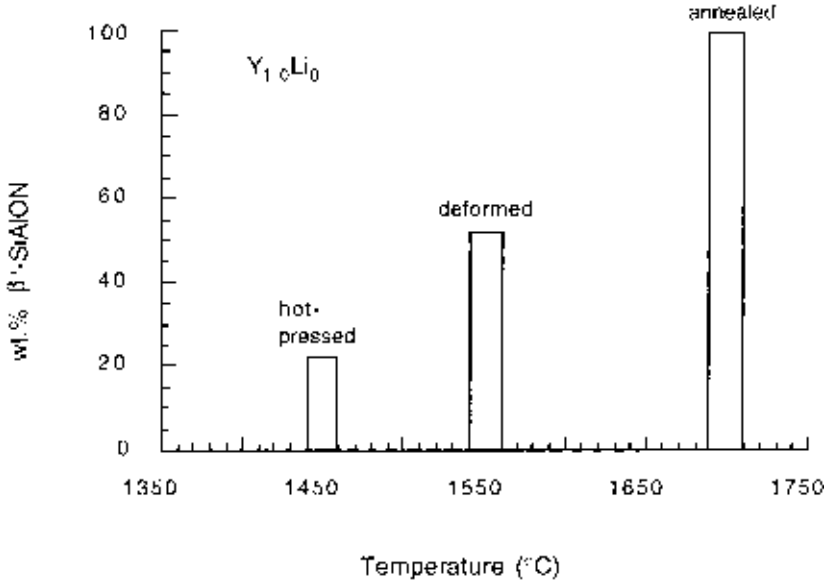

Fig. 3. Phase development during hot pressing, forming, and postforming annealing for the $Y_{1.0}Li_0$ material.

increases as the lithium content increases. Below the transition stress, which is relatively temperature insensitive, the temperature increase from 1550°C to 1575°C leads to a significant decrease in flow stresses, even though these temperatures are only 25°C apart. For example, compare the flow stress data at 10^{-3} s^{-1} in Fig. 8. Such a strong dependence of flow behavior may be attributed to the high activation energy of the viscosity of the grain-boundary phase in nitrogen-containing Si_3N_4 ceramics. Typical values of the activation energy in these materials are in the range of 550 kJ/mol[7] to 890 kJ/mol.[16]

(3) Punch Stretching

(A) Forming Load: Punch stretching was performed at temperatures in the range of 1500°–1600°C at punch-displacement rates that vary over the range of 0.2–1 mm/min. A set of load–displacement curves for the $Y_{1.0}Li_0$ material that has been deformed at different temperatures and forming rates is presented in Fig. 9 (a sketch of a punch-stretching experiment is shown in the inset). For comparison, these curves are presented in a normalized form by normalizing the nominal pressure ($P/(Rh_\circ)$, where P is the punch load, R the punch radius, and $h_\circ$ the initial specimen thickness) by the reference flow stress, the latter taken from compression tests that have been performed at the same temperature at an ε value that is similar to the average punch-stretching strain rate. The punch displacement also has been normalized by the sum $R + h_\circ$. According to the analysis of Wu and Chen,[11,17] the observed increase in the normalized load is primarily caused by the increasing contact area between the punch and the workpiece and, secondarily, and very importantly, by increasing true strain rate of punch stretching, even though the punch speed remains constant. Because all these normalized curves fall onto one unique curve, which is quite similar to the one predicted by Xu and Chen[11] and Xu,[17] it is reasonable to assume that forming operations all occur under essentially comparable mechanical conditions, with flow stress as the main normalizing parameter. Furthermore, one may assert that, essentially, the same flow stress that was encountered in the uniaxial compression tests is encountered in these biaxial stretching experiments.

(B) Rupture Stress: In the actual experiments, each test was terminated when a sudden load decrease occurred. Invariably, subsequent examination found that at least a crack had formed at this stage. We have estimated the rupture stress by returning to the theoretical analysis,[11,17] which predicts that the flow stress during punch stretching increases monotonically, because of the increase of the average true strain rate. Thus, the final flow stress just prior to specimen fracture corresponds to the rupture stress, σ_r, of the material, which is given by[11,17]

$$\sigma_r = \frac{P}{2\pi R h_f \sin^2 \alpha} \tag{1}$$

Here, P is the recorded load just prior to the load decrease, R the punch radius, h_f the shell thickness at the rupture (measured at the rupture location), and α the half angle subtended by the punch contact from the center of the punch at the moment of rupture (which was measured by examining the contact marking on each failed specimen after the test). Strictly speaking, this stress value corresponds to the radial stress at the edge of the punch contact region rather than at the rupture location. However, a detailed analysis performed by Xu[17] showed that the stress state in the entire punch contact region is almost one of balanced biaxial tension. Numerically, similar stresses exist everywhere except at the pole and several millimeters away from it, where the stresses are, respectively, slightly lower and higher, because of punch friction. If we disregard these systematic differences, then the stress value calculated from Eq. (1) can be taken as a good approximation of the average radial stress in the stretched material, and it may be conveniently used to compare the rupture stresses of different materials or of the same material at different temperatures.

Table III shows the calculated rupture stresses of the $Y_{1.0}Li_0$ material that has been punch stretched at different forming rates and temperatures. As is evident from this table, the rupture stress is mostly independent of temperature and strain rate. (The same data are shown again in Fig. 10(a) for later comparison.) Calculated rupture stresses for other materials show the similar feature of temperature and strain-rate independence. However, the rupture stress is strongly material dependent and varies systematically with the yttrium/lithium composition. When the composition is changed from $Y_{1.0}Li_0$ to $Y_0Li_{1.0}$, σ_r decreases from a value of 25 MPa to a value of 16 MPa (Fig. 10(b)).

(C) Formability: Formability was evaluated by the distance of punch travel before rupture occurred. To compare the formability of different materials, a fixed deformation schedule of 0.8 mm/min at 1550°C was used. Formability initially increased as the lithium content increased, up to a composition of $Y_{0.66}Li_{0.33}$, after which it decreased significantly, with the $Y_0Li_{1.0}$ composition being essentially unformable (Fig. 11(a)). The temperature dependence of the formability is observed in Fig. 12(a) for the $Y_{1.0}Li_0$ composition and a forming speed of 0.6 mm/min. The formability improved monotonically as the temperature increased, up to 1600°C.

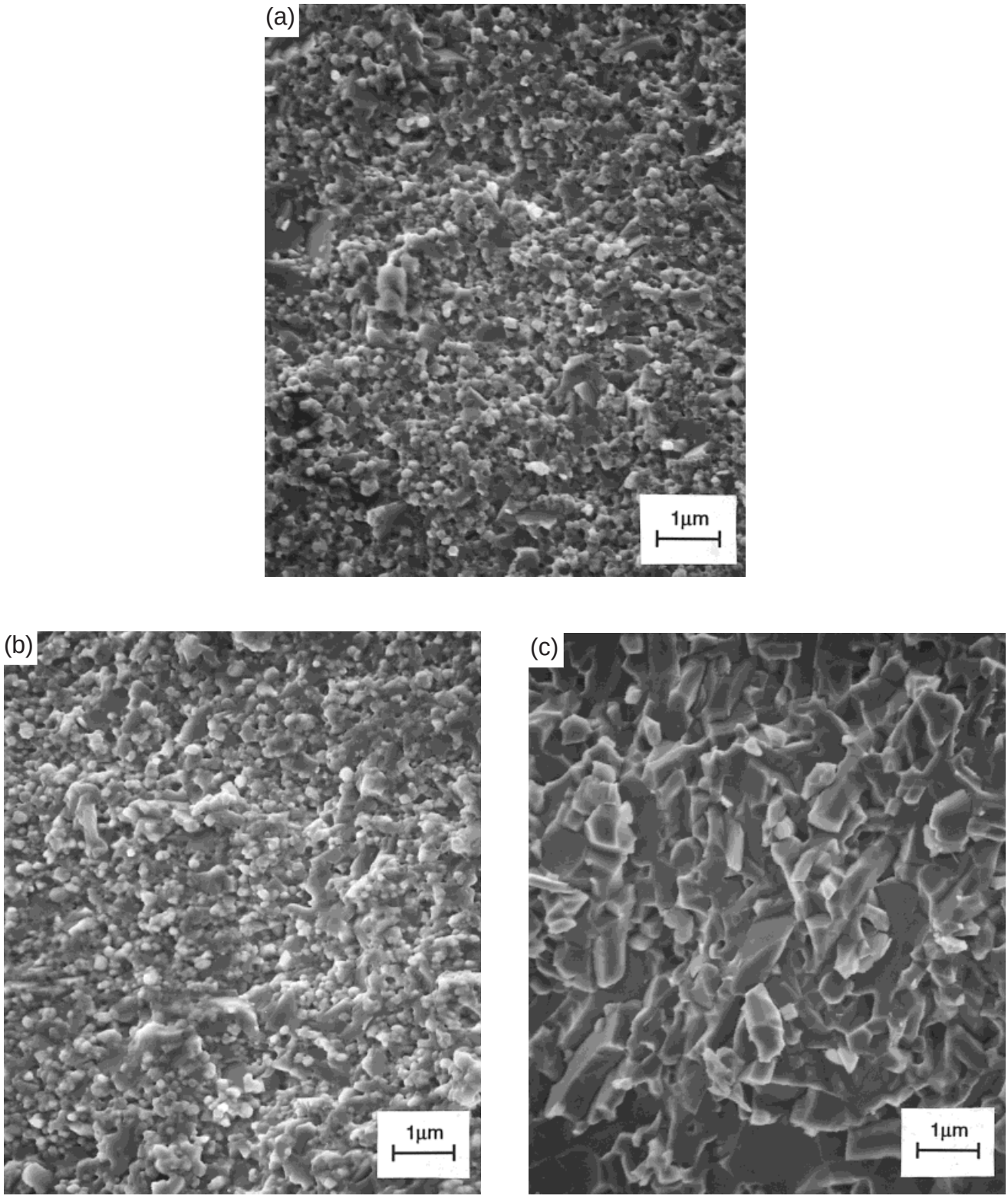

Fig. 4. SEM micrographs of fracture surfaces of the $Y_{1.0}Li_0$ material ((a) hot pressed at 1470°C, (b) punch stretched at 1585°C with a punch speed of 0.8 mm/min, and (c) annealed at 1700°C for 3 h).

To put the above-mentioned results into perspective, we also have plotted the σ_r/σ^*_{flow} ratio as a function of the lithium content in Fig. 11(b). Here, σ_r is taken from Fig. 10(b) and σ^*_{flow} is the reference flow stress, taken from the compression experiment for the same material at a fixed strain rate of 1.15×10^{-3} s^{-1}, which corresponds to the average strain rate during punch stretching at a forming speed of 0.8 mm/min. This average strain rate is computed by simply dividing the true strain of ~0.69 (100% engineering strain) by the time required to achieve this level of deformation. (We recall that the actual strain rate in punch-stretching increases as the punch travel increases.) Similarly, in Fig. 12(b), we plot the σ_r/σ^*_{flow} ratio for the $Y_{1.0}Li_0$ material as a function of temperature (for this plot, the value of σ_r has been taken from Table III and the value of σ^*_{flow} has been taken from the compression experiments that were performed at a strain rate of 8.6×10^{-4} s^{-1} at the corre-

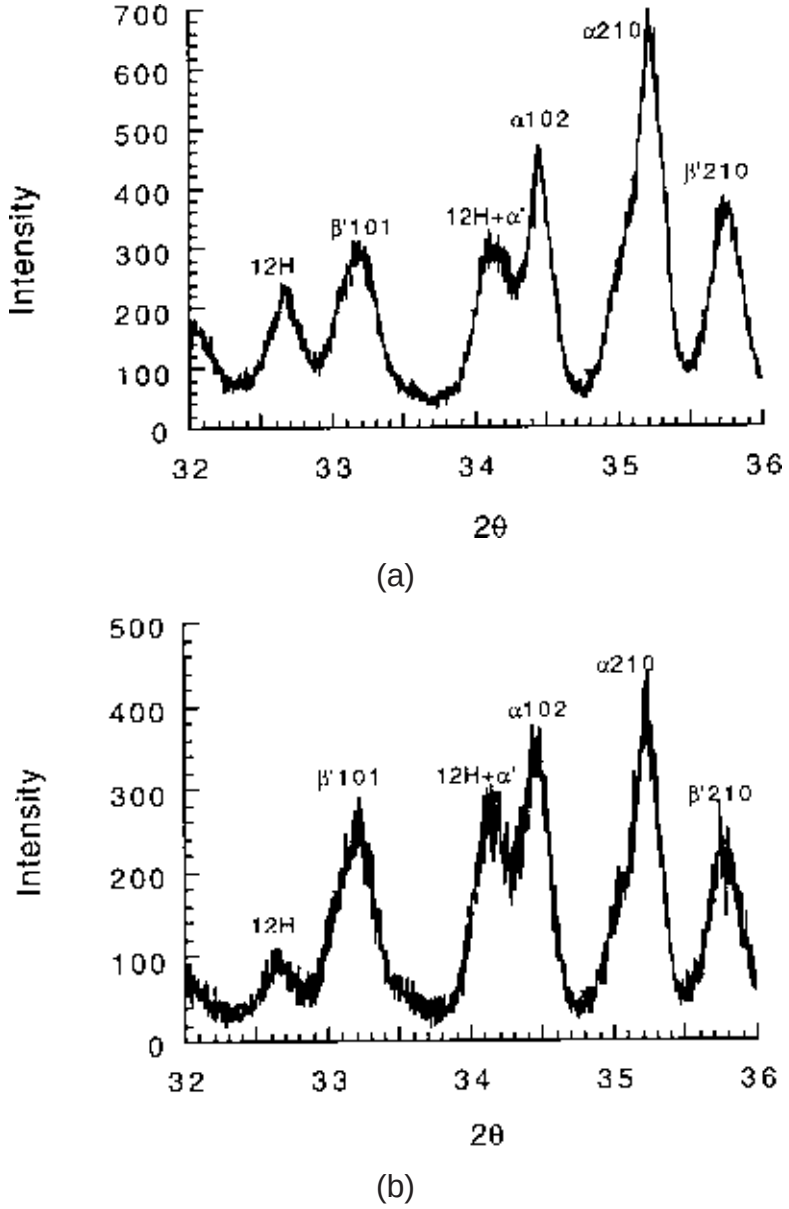

Fig. 5. XRD patterns of the $Y_{1.0}Li_0$ material punch stretched at a punch speed of 0.8 mm/min at 1585°C to a height of 10 mm ((a) as-deformed and (b) pulverized).

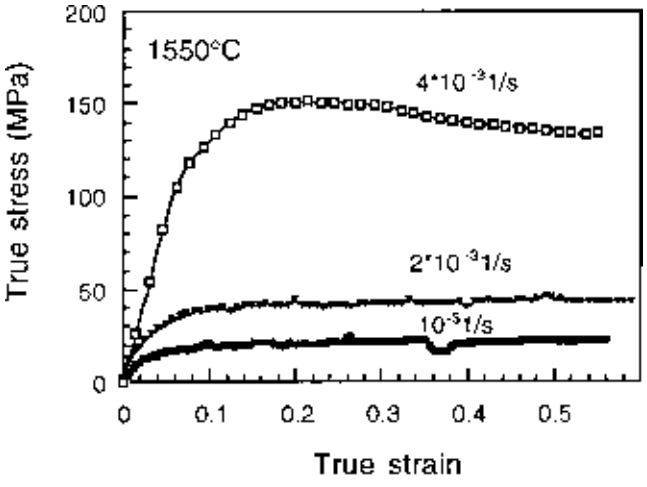

Fig. 6. True stress–true strain curves in compression for the $Y_{0.75}Li_{0.25}$ material.

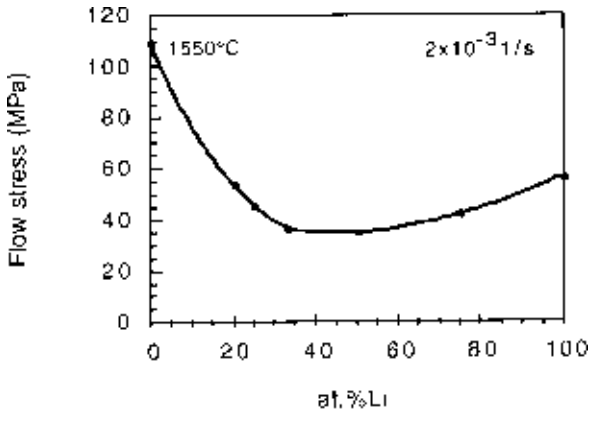

Fig. 7. True stress–true strain curves in the compression experiment for materials with different amounts of lithium cation.

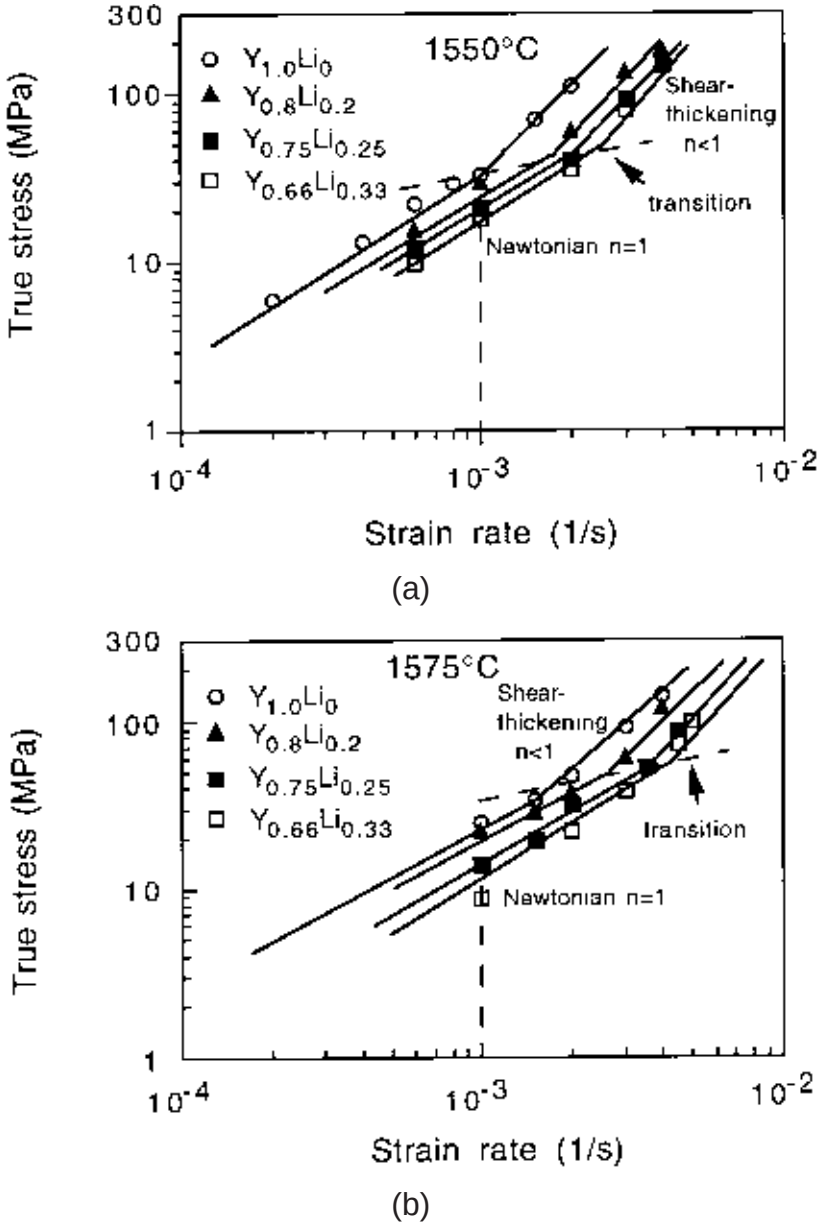

Fig. 8. Flow stress versus strain rate in compression for various materials at (a) 1550° and (b) 1575°C.

sponding temperatures). It is clear from Figs. 11 and 12 that the trend of σ_r/σ^*_{flow} is the same as that for formability. Because a high σ_r/σ^*_{flow} ratio implies that the flow stress at a given average strain rate is low compared to the rupture stress, it allows a longer punch travel to attain a higher final strain rate, at which point the flow stress exceeds the rupture stress and the material fractures.

The relevance of the rupture-to-flow-stress ratio as an indicator of the overall formability is further demonstrated in Fig. 13. This plot includes data from Figs. 11 and 12, as well as the rupture data that was obtained from other punch-stretching experiments that, for lack of space, are not described here. For each data point, the reference flow stress for a given material has been taken from compression experiments that were performed at the same temperature and the strain rate corresponding to the average strain rate of punch stretching. Overall formability (presented in the normalized form) is observed to increase continuously as the rupture-to-flow-stress ratio increases.

(D) Fracture Appearance: Two modes of fracture were commonly observed in this study (Fig. 14). In materials that were rich in yttrium ($Y_{1.0}Li_0$ to $Y_{0.5}Li_{0.5}$), fracture usually occurred through the formation of a single crack running across the entire dome. In materials that were rich in lithium ($Y_{0.25}Li_{0.75}$ and $Y_0Li_{1.0}$), multiple cracks formed at an earlier stage of stretching, leading to premature fracture. Notably, cracks in both cases originated slightly away from the pole and propagated circumferentially.

The fracture location observed here may be explained by the friction between the punch and the material at the pole. A detailed calculation of stress distributions for punch-stretching experiments,[17] based on a numerical formulation,[18] shows that, for our geometries, the maximum tensile strain and stress (in the radial direction) are located at the pole at the early stages of forming; as forming proceeds, they move progressively away from the pole, because of the friction between the punch and the material at the pole.[17,18] Assuming that fracture is caused by the maximum tensile stress, our observation of the fracture initiation at a short distance from the pole can be understood.

Regarding the effect of composition, we believe that premature fracture in the lithium-rich materials was due to the loss of lithium from the surface, which led to a higher flow stress there. Stress concentration then caused the rupture stress to be exceeded first on the surface, leading to multiple crack formation over a large region.

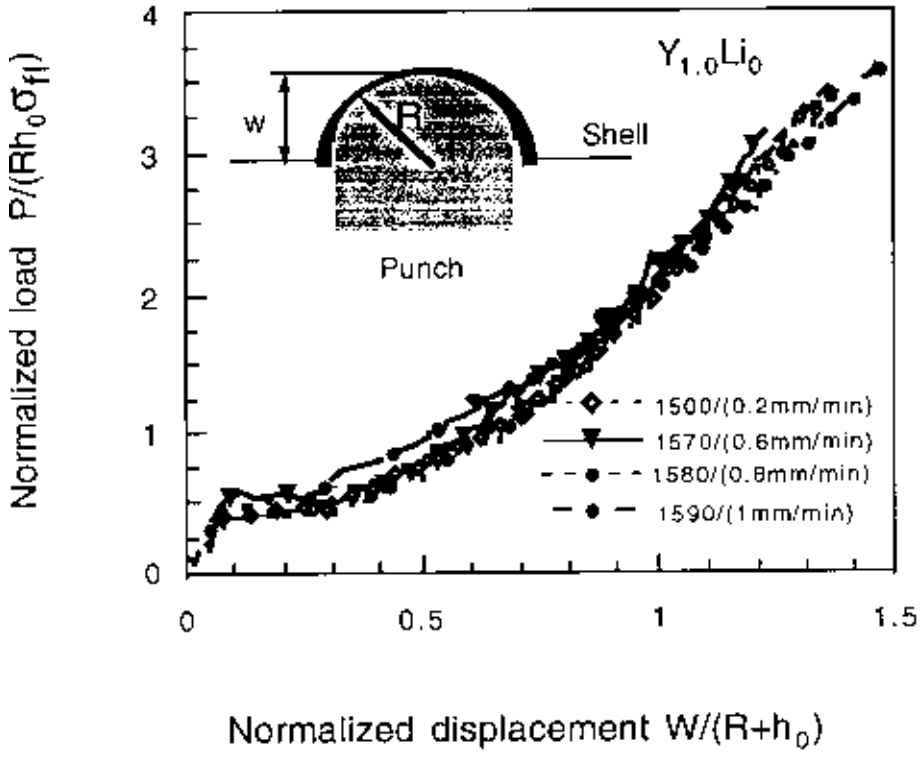

Fig. 9. Normalized load–displacement curves for the $Y_{1.0}Li_0$ material; a sketch of the punch-stretching setup is shown in the inset.

Table III. Rupture Stresses for $Y_{1.0}Li_0$ Material in Various Punch-Stretching Schedules

Temperature (°C)	Punch speed (mm/min)	Strain rate at rupture (s^{-1})	Rupture stress (MPa)
1500	0.2	2.3×10^{-4}	27
1550	0.4	5.7×10^{-4}	25.4
1570	0.6	8.6×10^{-4}	25
1585	0.8	1.15×10^{-4}	24.8
1600	1.0	1.44×10^{-4}	24.7

It is finally noted that shear thickening was probably not relevant in punch-stretching experiments. The highest stress at the end of punch stretching seemed to lie somewhat below the transition stress for shear thickening of the material, especially when the lithium content increased. Thus, superplastic punch stretching of these SiAlON materials can be described by the Newtonian flow mechanism that has a stress exponent $n = 1$.

(4) Hardness and Bend Strength at Room Temperature

Hardness of the as-hot-pressed materials was higher than that of materials after annealing. The higher the amount of yttrium in the composition, the greater the difference (Fig. 15(a)). On the other hand, bend strength, shown in Fig. 15(b), was higher for annealed materials; the difference is compositionally independent.

IV. Discussion

(1) Microstructure and Flow Stress

In this work, we have demonstrated that, through judicious processing, Si_3N_4 ceramics with equiaxed grains of primarily α-phase type can be prepared. During superplastic deformation, these ceramics undergo only a small amount of $\alpha \rightarrow \beta'$ phase transformation, and the resultant β′-SiAlON remains mostly equiaxed. The small amount of transformation also dictates that the crystallographic texture is weak in the present material. Overall, therefore, these ceramics satisfy the microstructural requirement for classical superplasticity and, indeed, large deformation at relatively high strain rate has been obtained. As discussed in Section III*(3)(D)*, biaxial tensile superplasticity is observed within the Newtonian regime, with a stress exponent *n* of approximately unity. This observation is reasonable, considering the amount and the importance of the liquid phase in Si_3N_4 ceramics. Indeed, superplasticity in ceramics that contain crystallites that are enveloped in a liquid matrix, such as β-$LiAlSi_2O_6$[1] and SiAlONs,[7] are often found to deform in the Newtonian regime with a stress exponent *n* of approximately unity, in contrast to crystalline ceramics (e.g., ZrO_2 and Al_2O_3), which have $n \approx 2$.[4,19,20] This strongly suggests that the superplastic deformation in Si_3N_4 ceramics is controlled by the liquid surrounding the grains.

Raj and Chyung[21] suggested that liquid-enhanced deformation in fine-grained ceramics can be controlled by interface reaction or by diffusion in the liquid. For the present experiments, which have studied a relatively broad range of composition, temperature, and strain rate, it would seem that interface control cannot be dominant in all cases and that diffusion control is more likely. This conclusion also is consistent with the decrease of flow stress with an increase in the lithium content, because the viscosity of glassy liquid is probably lowered by the addition of lithium, given the well-known effect of lithium as a glass modifier. On the other hand, diffusion-controlled, solution–reprecipitation creep is expected to have an inverse cubic dependence of the flow stress on the grain size in the Newtonian regime. Although the dynamic grain size evolution in the material that has been studied here has not been quantified, the grain size seems to increase somewhat during deformation. Yet, very little strain hardening or flow stress increase seems apparent in our experience. We suggest that the reason for the apparent constant flow stress could be a small decrease of viscosity of the liquid, which, in turn, could reflect a decrease of the nitrogen:oxygen ratio in the glass. This may be rationalized by the evolution of nitrogen supersaturation during phase transformation, in that an initially larger supersaturation exists at the beginning of the $\alpha \rightarrow \beta'$ phase transformation, which is gradually dissipated as the transformation proceeds. However, the verification of this speculation remains to be provided by future investigation.

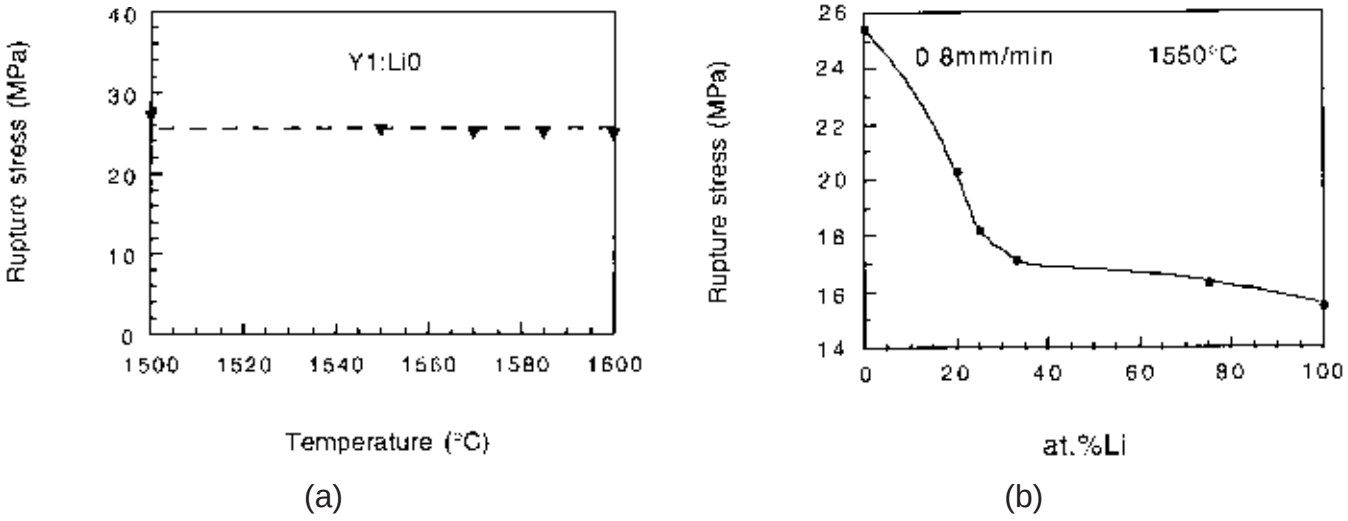

Fig. 10. Rupture stress in punch stretching ((a) $Y_{1.0}Li_0$ material at different temperatures and strain rates, as shown in Table III, and (b) materials with different lithium contents, all at 1550°C and a punch speed of 0.8 mm/min).

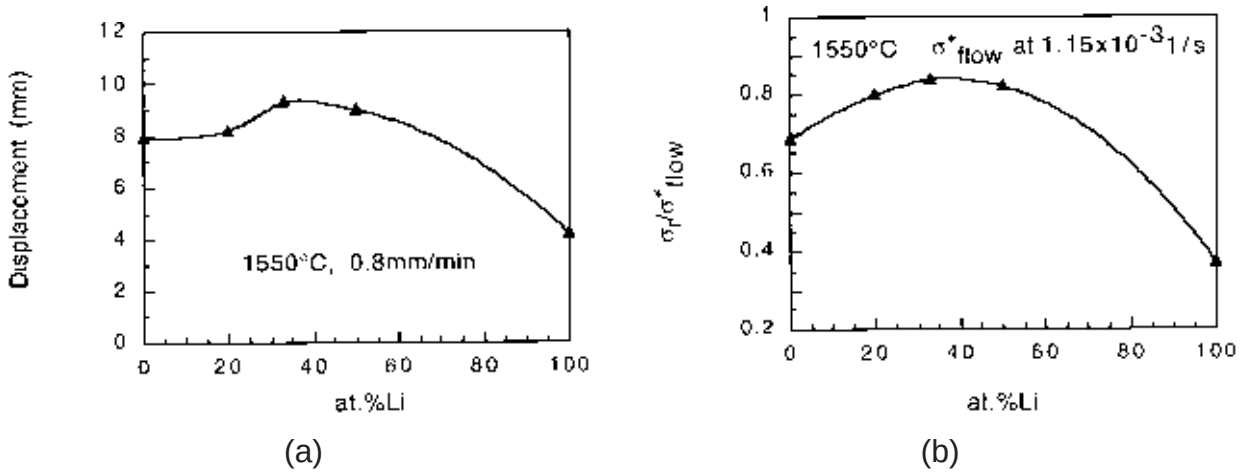

Fig. 11. (a) Total punch displacement versus lithium content, at 1550°C and a punch speed of 0.8 mm/min; (b) rupture-to-flow-stress ratio versus lithium content.

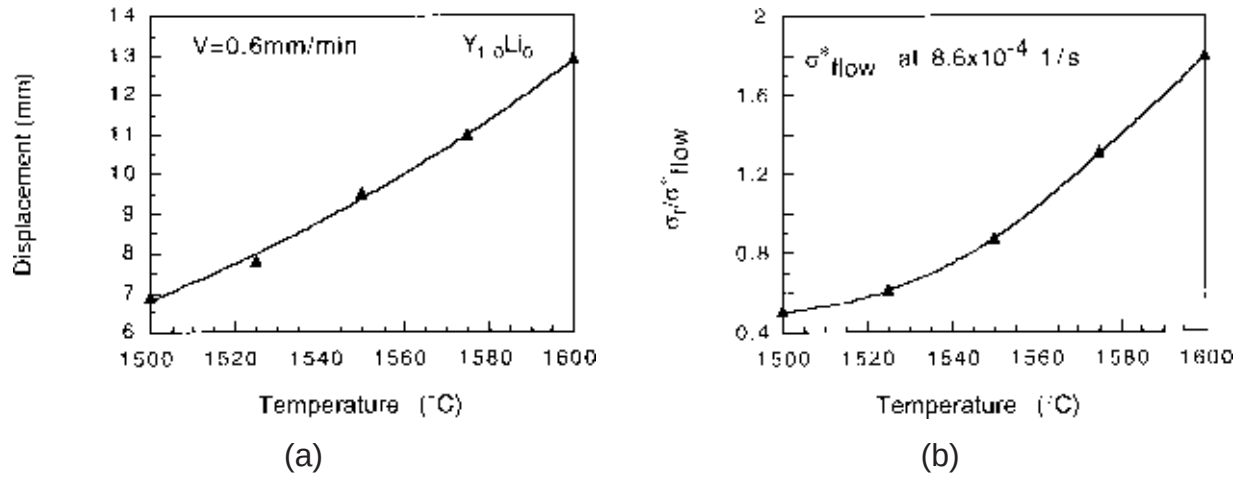

Fig. 12. (a) Total punch displacement of the $Y_{1.0}Li_0$ material versus temperature, at a punch speed of 0.6 mm/min; (b) rupture-to-flow-stress ratio as a function of temperature for the same material.

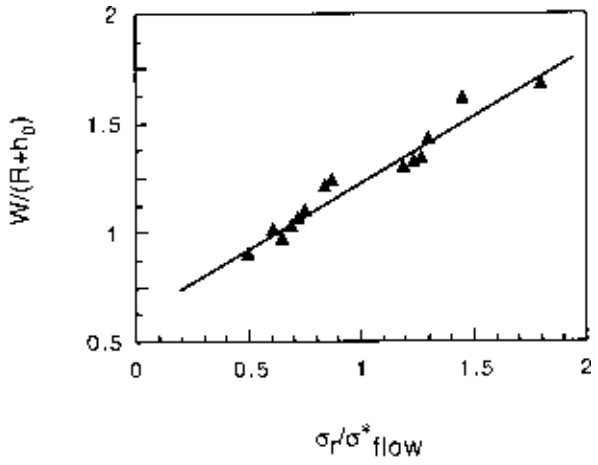

Fig. 13. Normalized displacement versus rupture-to-flow-stress ratio for a series of materials tested in punch stretching under various forming conditions.

(2) Fracture Stress

Perhaps the most interesting aspect of the present study is the confirmation of a critical stress beyond which fracture occurs, even in superplastic ceramics. This critical stress is material dependent but is otherwise independent of deformation conditions. It is generally on the order of ~25 MPa. This value is similar to the fracture stress that we obtained previously in tensile tests using superplastic SiAlON[7] and is in the same range of a variety of other superplastic ceramics, such as ZrO_2[22] and Al_2O_3.[23] Indeed, we have previously suggested that 20 MPa should be generally regarded as an upper bound of operational stress for superplastic ceramics beyond which large strain deformation cannot be sustained.[4,24]

Of course, superplastic fracture has a very different character from that of creep fracture of nonsuperplastic ceramics. Recent studies of tensile creep fracture of nonsuperplastic ceramics, especially those containing a substantial amount of liquid phase or a soft deforming phase, have firmly established that tensile strain is almost entirely attributable to cavitation,[25,26] and that creep life is inversely dependent on creep rate.[27] The latter result is sometimes represented in the form of the so-called Monkman–Grant relation, showing an essentially inverse creep life–creep rate dependence and a relatively constant ductility. This applies not only to creep fracture under a high stress in which n is very high (typically ≥5) and fracture origin can be traced to preexisting flaws,[26–28] but also to creep fracture under a low stress in which n is closer to unity (typically 2–3) and creep damage is diffuse, mostly unrelated to preexisting flaws.[28] For superplastic ceramics, the ductility is usually two orders of magnitude higher than that of typical creep fracture. Obviously, such strain cannot be associated with cavitation, although cavitation no doubt exists prior to final fracture. Preexisting defects also are obviously of no consequence. For example, we have not noted any dependence of the ductility on the surface finish of the specimens.

Clearly, fracture of superplastic ceramics is most likely due to cavitational damage that has nucleated and accumulated during deformation. Thus, the very distinct fracture stress is best interpreted as a threshold stress for cavitational damage. The origin of the stress threshold is not likely to be associated with the growth of cavities, which must occur for any that exceed a size of

$$r = \frac{2\gamma}{\sigma_\infty} \tag{2}$$

In the above, r is the radius of curvature of the cavity (spherical cavity surfaces are assumed), γ the surface tension, and σ_∞ the applied tensile stress. For the typical values of $\gamma = 1$ J/m^2 and $\sigma_\infty = 20$ MPa, we arrive at $r = 0.1$ μm. For well-sintered superplastic ceramics, which have a grain size of ~0.3 μm, pores of this size are few and their sizes and numbers are expected to vary considerably from material to material. Such variability is not consistent with the relatively constant fracture stress that is observed for superplastic ceramics.

To investigate whether the threshold stress results from cavity nucleation, we recall that nucleation theory dictates that a nucleation barrier given by

$$\Delta G^* = \left(\frac{16\pi\gamma^3}{3\sigma^{*2}}\right) f(\theta) \tag{3}$$

where the value of $f(\theta)$ is given by

$$f(\theta) = \frac{(2 + \cos\theta)(1 - \cos\theta)^2}{4} \tag{4}$$

must be surmounted to nucleate a lenticular cavity of dihedral angle 2θ and under a local tensile stress σ^* on the grain boundary. For typical ceramics that have $\theta \approx 60°$ and a nucleation barrier of $\Delta G^* \approx 60kT$, the stress that is required is on the order of

$$\sigma^* = 0.2\left(\frac{\gamma^3}{kT}\right)^{1/2} \tag{5}$$

or 1.25 GPa at 1550°C. This stress is clearly much higher than

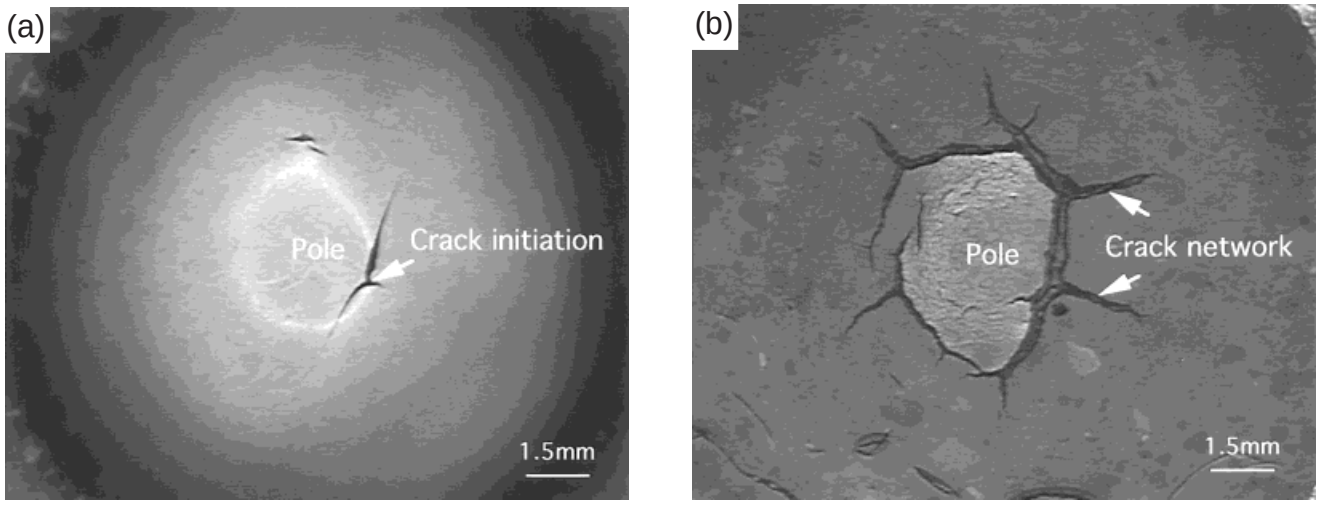

Fig. 14. Fracture modes during punch stretching at a punch speed of 0.4 mm/min and a temperature of 1550°C in (a) $Y_{1.0}Li_0$ materials (single crack forms prior to rupture) and (b) $Y_0Li_{1.0}$ materials (multiple crack formation precedes rupture).

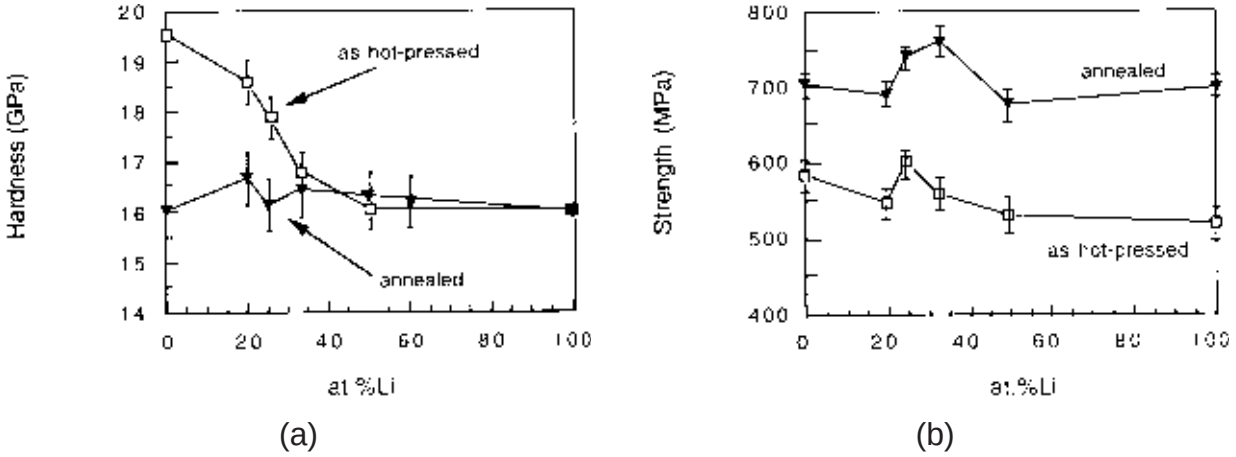

Fig. 15. (a) Hardness and (b) bend strength versus lithium content for as-hot-pressed and annealed materials.

the applied stress and can occur only as stress bursts because of deformation transients.[29,30] Stress bursts may occur at triple points or other stress concentrators when the local deformation pattern is abruptly perturbed, causing grain-boundary sliding, grain rotation, or grain separation, and are most severe at their inception when grains are only constrained elastically. Given a far-field applied stress σ_∞ and a characteristic length d, which may be taken as the grain size in a material that is free of grain-boundary precipitates, the burst in local stress is on the order of

$$\sigma^* = \sigma_\infty \left(\frac{d}{x}\right)^{1/2} \tag{6}$$

where x is the distance from the stress concentration. (Here, we adopted the elasticity solution for the stress distribution in front of the crack tip.[29,31,32]) This stress burst is later rapidly dissipated as the range of diffusional smoothing quickly overtakes the vicinity of stress concentration, lowering the local stress once again to σ_∞ as time proceeds. Using these values—σ_∞ = 20 MPa,◦σ^* = 1.2 GPa, and d = 0.5 μm—we find x to be 0.15 nm (1.5 A), i.e., on the order of the dimension of an atom.

The discussion above demonstrates that the threshold stress, if it is derived from nucleation conditions, is important, because it provides the minimum background stress on which potent stress bursts capable of cavity nucleation may occasionally build up. It has been argued in the literature of creep fracture of metals that the nature of stress bursts is stoichastic and it continues to occur at various locations within a polycrystal as creep deformation proceeds.[30] The threshold stress that is observed in metals varies more widely, possibly reflecting the wider range of grain size and grain-boundary morphology; however, it also lies in the range of several to tens of MPa units, including those for superplastic metals.[33] It would then seem that the basic origin of threshold stress that is observed in superplastic ceramics is possibly similar to that in metals. Given the fact that most parameters in Eqs. (5) and (6) are not sensitive to material classes, this finding is, perhaps, not surprising.

V. Conclusions

(1) SiAlON materials amenable to classical superplasticity were obtained when complete densification preceded the $\alpha \rightarrow \beta'$ phase transformation; this was achieved by using low temperatures and short holding times during the hot-pressing stage.

(2) Substitution of yttrium cations by lithium cations in $Y_{m/3}Si_{12-(m+n)}Al_{m+n}O_nN_{16-n}$ SiAlON resulted in a decreased viscosity of the grain-boundary phase and a decrease of the flow stress. Although Newtonian flow was generally observed at lower stresses, pronounced strain hardening was found in compositions rich in the lithium modifying cation, because of the high rates of lithium cation loss.

(3) High deformation rates—10^{-3} s^{-1} in compression and 1.2×10^{-3} s^{-1} in biaxial punch stretching—were achieved in these superplastic SiAlONs at intermediate lithium/yttrium compositions in the temperature range of 1450°–1625°C.

(4) Addition of the lithium modifying cation decreased the fracture stresses, whereas maximization of the σ_r/σ_{flow} ratio led to the highest formability. The material with the $Y_{0.66}Li_{0.33}$ composition was the most formable.

(5) All materials exhibited higher room-temperature bend strength after postforming annealing. Thus, transient superplastic deformation did not impair the ultimate mechanical properties of the materials.

References

[1]J.-G. Wang and R. Raj, "Mechanism of Superplastic Flow in a Fine-Grained Ceramic Containing Some Liquid Phase," *J. Am. Ceram. Soc.*, **67** [6] 399–409 (1984).
[2]F. Wakai, S. Sakaguchi, and Y. Matsuno, "Superplasticity of Yttria-Stabilized Tetragonal ZrO_2 Polycrystals," *Adv. Ceram. Mater.*, **1**, 259 (1986).
[3]L. A. Xue, X. Wu, and I-W. Chen, "Superplastic Alumina Ceramics with Grain Growth Inhibitors," *J. Am. Ceram. Soc.*, **74** [4] 842–45 (1991).
[4]I-W. Chen and L. A. Xue, "Development of Superplastic Structural Ceramics," *J. Am. Ceram. Soc.*, **73** [9] 2585–609 (1990).
[5]F. Wakai, Y. Kodama, S. Sakaguchi, N. Murayama, K. Izaki, and K. Niihara, "A Superplastic Covalent Crystal Composite," *Nature (London)*, **344**, 421 (1990).
[6]X. Wu and I-W. Chen, "Exaggerated Texture and Grain Growth in a Superplastic SiAlON," *J. Am. Ceram. Soc.*, **75** [10] 2733–41 (1992).
[7]S.-L. Hwang and I-W. Chen, "Superplastic Forming of SiAlON Ceramics," *J. Am. Ceram. Soc.*, **77** [10] 2575–85 (1994).
[8]T. G. Nieh and J. Wadsworth, "Dynamic Grain Growth during Superplastic Deformation of Yttria-Stabilized Tetragonal Zirconia Polycrystals," *J. Am. Ceram. Soc.*, **72** [8] 1469–72 (1989).
[9]C.-M. Hwang, "The Systems SiAlON–$Y_3Al_5O_{12}$ and SiAlON–Cordierite: Sintering and Grain Growth"; Ph.D. Thesis. Department of Materials Science and Engineering, University of Michigan, Ann Arbor, MI, 1988.
[10]I-W. Chen and S.-L. Hwang, "Superplastic SiAlON—A Bird's Eye View of Silicon Nitride Ceramics," *Mater. Res. Soc. Symp. Proc.*, **287**, 209–22 (1993).
[11]X. Wu and I-W. Chen, "Superplastic Bulging of Fine-Grained Zirconia," *J. Am. Ceram. Soc.*, **73** [3] 746–49 (1990).
[12]C. P. Gazzara and D. R. Messier, "Determination of Phase Content of Si_3N_4 by X-Ray Diffraction Analysis," *Am. Ceram. Soc. Bull.*, **56** [9] 777–80 (1977).
[13]S.-L. Hwang and I-W. Chen, "Reaction Hot Pressing of α′- and β′-SiAlON Ceramics," *J. Am. Ceram. Soc.*, **77** [1] 165–71 (1994).
[14]C. M. B. Henderson and D. Taylor, "Thermal Expansion of the Nitrides and Oxynitride of Silicon in Relation to their Structures," *Trans. J. Br. Ceram. Soc.*, **74** [2] 49–53 (1975).
[15]I-W. Chen and S.-L. Hwang, "Shear Thickening Creep in Superplastic Silicon Nitride," *J. Am. Ceram. Soc.*, **75** [5] 1073–79 (1992).
[16]T. Rouxel, H. Lemercier, and J.-L. Besson, "Rheological Behavior of YSiAlON Glasses—Its Incidence on the High-Temperature Deformation of Si_3N_4 Ceramics Sintered with Al_2O_3 and Y_2O_3 Additives"; pp. 175–85 in *Tailoring of Mechanical Properties of Si_3N_4 Ceramics*. Edited by M. J. Hoffmann and G. Petzow. Kluwer, Dordrecht, The Netherlands, 1994.
[17]X. Wu, "Deformation Processing of Ceramics"; Ph.D. Thesis. Department of Materials Science and Engineering, University of Michigan, Ann Arbor, MI, 1990.
[18]N. M. Wang, "Large Plastic Deformation of a Circular Sheet Caused by Punch Stretching," *J. Appl. Mech.*, **37** [6] 431–39 (1970).
[19]F. Wakai and T. Nagona, "The Role of Interface-Controlled Diffusion Creep on Superplasticity of Yttria-Stabilized Tetragonal ZrO_2," *J. Mater. Sci. Lett.*, **7** 607–609 (1988).

[20]R. M. Cannon, W. H. Rhodes, and A. H. Heuer, "Plastic Deformation of Fine-Grained Alumina (Al_2O_3): I. Interface-Controlled Diffusional Creep," *J. Am. Ceram. Soc.*, **63** [1–2] 48–53 (1980).

[21]R. Raj and C. K. Chyung, "Solution–Precipitation Creep in Glass Ceramics," *Acta Metall.*, **29**, 159–66 (1981).

[22]T. G. Nieh, C. M. McNally, and J. Wadsworth, "Superplastic Properties of a Fine-Grained Yttria-Stabilized Tetragonal Polycrystal of Zirconia," *Scr. Metall.*, **22**, 1297 (1988).

[23]P. Gruffel, P. Carry, and A. Mocellin, "Effect of Testing Conditions and Doping on Superplastic Creep of Alumina"; p. 587 in *Science of Ceramics, Vol. 14*. Edited by D. Taylor. The Institute of Ceramics, Shelton, Staffordshire, U.K., 1988.

[24]L. A. Xue and I-W. Chen, "Fabrication of Mullite Body Using Superplastic Transient Phase," *J. Am. Ceram. Soc.*, **75** [5] 1085–91 (1992).

[25]C.-F. Chen and T.-Y. Tien, "High Temperature Mechanical Properties of SiAlON Ceramics: Microstructural Effects," *Ceram. Eng. Sci. Proc.*, **8** [7–8] 778–95 (1987).

[26]W. Luecke, S. Wiederhorn, and B. Hockey, "Cavitation Contributes Substantially to Tensile Creep in Silicon Nitride," *J. Am. Ceram. Soc.*, **78** [9] 2085–96 (1995).

[27]S. M. Wiederhorn, B. J. Hockey, and D. C. Cranmer, "Transient Creep Behaviour of Hot Isostatically Pressed Silicon Nitride," *J. Mater. Sci.*, **28**, 445–53 (1993).

[28]T. Ohji, "Tensile Creep Rupture and Subcritical Crack Growth of Silicon Nitride"; see Ref. 16, pp. 175–85.

[29]A. S. Argon, I-W. Chen, and C. W. Lau, *Creep, Fatigue, and Environment Interactions*; p. 46. Edited by R. M. N. Pelloux and N. Stoloff. American Institute of Mining, Metallurgical, and Petroleum Engineers, Warrendale, PA, 1980.

[30]I-W. Chen and A. S. Argon, "Creep Cavitation in 304 Stainless Steel," *Acta Metall.*, **29**, 1321–33 (1981).

[31]C. W. Lau and A. S. Argon, "Stress Concentrations Caused by Grain-Boundary Sliding in Metals Undergoing Power-Law Creep"; pp. 595–601 in *Fracture 1977, Vol. 2*. Edited by D. M. R. Taplin. University of Waterloo Press, Waterloo, Canada, 1977.

[32]A. G. Evans, J. R. Rice, and J. P. Hirth, "Suppression of Cavity Formation in Ceramics: Prospects for Superplasticity," *J. Am. Ceram. Soc.*, **63** [7–8] 368–75 (1980).

[33]J. Wadsworth and O. D. Sherby, "Overview: Superplasticity and Superplastic Forming Processes," *Mater. Sci. Technol.*, **1**, 925–36 (1985). □